

The spectral evolution of impulsive solar X-ray flares

Paolo C. Grigis and Arnold O. Benz

Institute for Astronomy, ETH Zürich, CH-8092 Zürich

Received 28 May 2004 / Accepted 15 July 2004

Abstract. The time evolution of the spectral index and the non-thermal flux in 24 impulsive solar hard X-ray flares of GOES class M was studied in RHESSI observations. The high spectral resolution allows for a clean separation of thermal and non-thermal components in the 10–30 keV range, where most of the non-thermal photons are emitted. Spectral index and flux can thus be determined with much better accuracy than before. The spectral soft-hard-soft behavior in rise-peak-decay phases is discovered not only in the general flare development, but even more pronounced in subpeaks. An empirically found power-law dependence between the spectral index and the normalization of the non-thermal flux holds during the rise and decay phases of the emission peaks. It is still present in the combined set of all flares. We find an asymmetry in this dependence between rise and decay phases of the non-thermal emission. There is no delay between flux peak and spectral index minimum. The soft-hard-soft behavior appears to be an intrinsic signature of the elementary electron acceleration process.

Key words. Sun: flares – Sun: X-rays, gamma rays – Acceleration of particles

1. Introduction

Non-thermal hard X-ray emission during impulsive solar flares is highly variable, often showing activity peaks and dips with durations ranging from seconds up to several minutes. This behavior can be observed in the largest X class flares as well as in smaller B and C class flares. It was early recognized (Parks & Winckler 1969; Kane & Anderson 1970) that the hardness of the photon spectrum can also change with time, and, furthermore, that there is a direct correlation between the hard X-ray flux and the spectral hardness. Since this implies that the flare spectrum starts soft, gets harder as the flux rises and softer again after the peak time, the term *soft-hard-soft* (SHS) was coined to describe this behavior. Later observations of major flares (Benz 1977; Brown & Loran 1985; Lin & Schwartz 1986; Fletcher & Hudson 2002; Hudson & Fárník 2002) confirmed the SHS pattern. However, flares were also observed that systematically hardened with time (Frost and Dennis 1971; Cliver et al. 1986; Kiplinger 1995), thus showing a *soft-hard-harder* (SHH) pattern. Current wisdom suggests that SHH flares represent gradual, long duration events. These are much less frequent than impulsive events.

The non-thermal photons usually follow a power-law distribution in energy. The power-law index, γ , can be directly related to the energy distribution of the electron flux impinging on the target (assuming a model for the bremsstrahlung emission), and implicitly to the acceleration process. The evolution of spectral index and flux reflects a development in the accel-

erator. Thus, the relation between index and flux is an observational constraint for acceleration theories.

While it seems to be well established that impulsive flares have an SHS spectral dynamic, much less is known about the *quantitative* relation, if any, between the photon spectral index and the non-thermal X-ray flux during the burst. The Reuven Ramaty High-Energy Solar Spectroscopic Imager (RHESSI) spacecraft (Lin et al. 2002), which observes hard X-rays and γ -rays from the sun, is ideally suited to explore this relation. Its key features of high spectral resolution (1 keV in the X-ray range) and coverage of the low-energy range (down to 3 keV) allow us to separate the thermal continuum from the non-thermal component of the spectrum, to study also the 10–30 keV region where most of the non-thermal photons are emitted, to identify and account for peculiar spectral features (like breaks in the power-law etc.), and to follow the evolution of the non-thermal part right from the onset of the flare. Therefore, the spectral index and flux of RHESSI non-thermal photons can be studied with much higher precision than previously.

This paper presents a large set of measurements of the non-thermal component from 24 different solar flares and investigates quantitatively the relation between the non-thermal flux and the spectral index. The flares were selected in such a way as to represent the class of impulsive flares with strong non-thermal emission. In Section 2 we give a detailed description of the selection and data reduction process that yields the dataset which is then analyzed in Section 3 and discussed in Section 4.

2. Observations and Data Reduction

Our main observational goal is the accurate study of the time evolution of the spectral index γ and the non-thermal X-ray flux in a representative sample of solar flares, using data from RHESSI. In this section we give a detailed account of the different steps that were undertaken in the data analysis process, starting from the event selection.

2.1. Event selection

The event selection has to be very careful in order to pick a representative collection of flares. Ideally, one would analyze all the observed events or a randomly chosen subset thereof. In practice, however, instrumental issues reduce the freedom of choice, since not all the events are equally suitable for the different tasks of high precision spectral analysis. A detailed discussion about the RHESSI onboard detectors and their use for spectroscopy can be found in Smith et. al. (2002). We limited our analysis to flares having a peak soft X-ray flux larger than GOES class M1 and smaller than X1. These have fairly large count rates, but are not too heavily affected by pulse pileup. 176 M-class flares were reported in the RHESSI flare list in the period from 13 February 2002 to 31 November 2002. From this collection we restricted our analysis to the 79 flares observed with a constant attenuator state of 1 (thin attenuator in) and no front-segment decimation. Therefore we do not need to deal with attenuator motions and decimation state changes during the flare, and we have the best conditions for spectroscopy of M-class flares.

From this selection of 79 flares we dropped the ones which had no emission above the background in the 25–50 keV band, as determined by visual inspection of the observing summary light curves. Since we expect the bulk of the thermal radiation from M-class flares to be emitted mostly below 25 keV, this condition introduces a bias toward flares with substantial non-thermal emission. This is not a severe restriction, since we want to study specifically the non-thermal emission, and it would be very hard to ascertain the properties of any weak non-thermal emission anyway. In order to have enough data for meaningful time series, we additionally required the peak in the 25–50 keV band being more than 3 minutes away from any interruption in the data, as caused by the spacecraft entering or leaving the shadow of the Earth, the South Atlantic Anomaly (SAA), etc. We also dropped the events in which charged particle precipitation significantly increased the background counts during the time of enhanced emission in the 25–50 keV band. These additional criteria dropped the number of events to 32.

2.2. Data reduction and analysis

For each event in the list, we determined:

- A contiguous time interval of sunlight containing the event without data gaps.
- The peak time of the observing summary count light curve in the energy band 25–50 keV.
- The RHESSI rotation period at peak time.
- The location of the source on the sun.

The flare locations were taken from the automatically computed positions given by the RHESSI Experimental Data Center (HEDC) (Saint-Hilaire et. al. 2002). Visual inspection of the corresponding images confirmed that in all cases correct and accurate positions were given, with the exception of 3 flares for which the RHESSI aspect solution (Fivian et. al. 2002; Hurford & Curtis 2002) quality was insufficient to permit reconstruction of meaningful images. We then proceeded to generate RHESSI count spectrograms for each flare in the uninterrupted sunlight time interval, with a time binning equal to the spin period at peak time (which in all cases is very close to 4 s) and an energy binning of 1 keV from 3 to 6 keV, 0.33 keV from 6 to 13 keV, 1 keV from 13 to 36 keV, 2 keV from 36 to 60 keV, 5 keV from 60 to 120 keV, 10 keV from 120 to 200 keV, 20 keV from 200 to 300 keV. Pileup correction was enabled with a deadtime threshold of 5%. We only used the front segments of the detectors, and systematically excluded the detectors 2 and 7, which have lower energy resolution. For some flares we also excluded detector 8 (which does not deliver good data when the onboard transmitter is active). The full spectral response matrix (SRM) was computed for each spectrogram, using the HEDC flare positions to enable position dependent corrections for the flares whose position was known. We discarded 2 events for which we were unable to generate the SRM.

To derive the spectral indices for the spectra, we use the forward fitting method implemented by the SPEX code (Schwartz 1996; Smith et al. 2002). The procedure requires the user to choose a model photon spectrum, which is multiplied with the instrument response matrix and then fitted to the observed count spectrum. The best-fit parameters are given as output. To obtain the time evolution of the parameters, the fitting procedure is performed for each time bin in the spectrogram of the time interval of interest. We have chosen to use a photon spectral model featuring a power-law with a low-energy turnover in addition to a thermal thick-target bremsstrahlung emission. The negative power-law index below the low-energy turnover was fixed at 1.5. Hence there are 5 free parameters in the model: the temperature T of the assumed isothermal emission and its emission measure \mathcal{M} ; for the non-thermal component the power-law index γ , the normalization of the power-law F_{E_0} at the (fixed) normalization energy E_0 and the low-energy turnover E_{turn} . The non-thermal part of the spectrum is thus given by

$$F(E) = \begin{cases} F_{E_0} \left(\frac{E}{E_0}\right)^{-\gamma} & E > E_{\text{turn}} \\ F_{E_0} \left(\frac{E_{\text{turn}}}{E_0}\right)^{-\gamma} \left(\frac{E}{E_{\text{turn}}}\right)^{-1.5} & E < E_{\text{turn}} \end{cases} \quad (1)$$

An example photon spectrum with an overlay of the best-fit model is shown in Fig. 1. For all the events we selected background time intervals (preferentially before and after the flare) in each of the following 4 energy bands: 3–12, 12–30, 30–60, 60–300 keV. The counts in the different background intervals were then fitted to a polynomial of degree varying from 0 to 3, which was used to interpolate the background intensity during the event. We defined then the *fitting time interval* as the time when the emission in the band 30–60 keV was significantly above the background level.

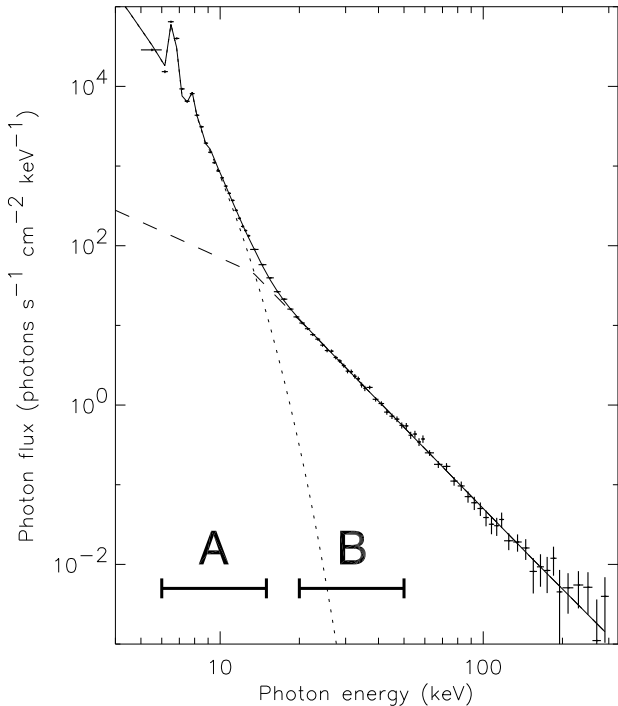


Fig. 1. A RHESSI photon spectrum for 9 November 2002 at 13:14:16 UT, integrated over one rotation period of approximately 4 s. Overlaid on it, an isothermal thick-target bremsstrahlung emission (dotted line) with temperature $T = 16.7$ MK and emission measure $\mathcal{M} = 7.54 \cdot 10^{48} \text{ cm}^{-3}$, a power-law (dashed line) with spectral index $\gamma = 3.39$ and normalization $F_{50} = 0.525$, and a low-energy turnover $E_{\text{turn}} = 13.4$ keV. The continuous line represents the sum of these two components.

2.3. Automatic spectral fitting

A time dependent determination of the model's best-fit parameters for 30 flares lasting a few minutes with 4 s data bins requires more than thousand fittings. To reduce the burden of the work involved in the data analysis, we implemented an automatic fitting procedure. However, automatic procedures have their own drawbacks, in particular if the fitting happens to converge towards a wrong local minimum of χ^2 , sometimes giving as a result spectacularly wrong fittings. We decided to settle for the following compromise: we let the fittings be computed automatically, but we visually inspected the results afterwards, and eliminated then the obviously wrong ones without making any attempt to recompute them. As a matter of fact, we iterated the procedure described above for a few rounds, each time improving the automatic fitting routine. After the last run we had to discard only a few fittings at the beginning and at the end of some fitting time intervals. Here follows a basic description of the algorithm used by the automatic fitting routine:

1. A fitting of T and \mathcal{M} for an isothermal emission is made in the low-energy range A shown in Fig. 1, where one can safely assume that the thermal emission is dominant.

2. The range for the initial fit of the non-thermal part is defined as B in Fig. 1. If the emission does not exceed 0.1 photons $\text{s}^{-1} \text{ cm}^{-2} \text{ keV}^{-1}$ or five times the thermal emission as found in step 1, the range of the fit is reduced to the interval where it does satisfy these conditions.
3. A photon spectral model with a fixed thermal emission with T and \mathcal{M} as found in step 1 and a (not broken) power-law is fitted in the non-thermal range defined in step 2.
4. The parameters resulting from step 1 and 3 are used as initial estimates for the final fitting of all the 5 free parameters of the model to the spectrum in the energy range 6–150 keV. The low-energy turnover initial estimate is taken as either the fitted E_{turn} from the previous spectrum in the time sequence, or a default value.

We emphasize that the first steps described above only provide the initial estimates for the parameters, which are then let *totally free* in the last fitting over the whole energy range. Steps 1–3 simply attempt to give reasonable initial guesses for the parameters. The energy ranges A and B and the default values used by the routine are fixed and were determined empirically to achieve the largest possible number of good fittings. We have experimented with alternative spectral models. They included for example models with a slightly hotter isothermal component, or two components of thermal emission, but no non-thermal emission. Such models fit the observed spectra with similar values of χ^2 , when the power-law index γ is greater than about 8.

2.4. Best-fit parameters selection and results

The automatic fitting routine failed to provide results for 4 events. Its output consists of the best-fit parameters for a total of 1 566 spectral fittings from 26 events. The visual inspection of all the fittings allowed us to eliminate the spectra which were badly fitted because they would have required a broken power-law model. We also chose to discard all the spectra whose power-law component had an index similar to the logarithmic derivative of the thermal emission around the energy at which it was only about as strong as the background, because in such a case it is very difficult to ascertain the reality of any non-thermal emission. After the selection process explained above, we were left with a total of 911 fittings for 24 events, spanning a total time of 3 722 s. The number of fittings for each event ranges from 5 to 212, with an average of 38. The 24 events with at least 5 good fittings are our final selection. They are listed in Table 1. Each fit consists of the 5 parameters T , \mathcal{M} , γ , F_0 and E_{turn} . All events are relatively short, have often many peaks and comply with the definition of impulsive flares.

Fitting free parameters to data may introduce hidden dependencies between them. It is important for the study of the index-flux relation to assess the effect of the fitting procedure. For this purpose we have compared the index-flux relation before and after fitting. For the flare of 9 November 2002 (the one with the longest time series) we computed two supplementary time series for the flux and spectral index from the uncalibrated count-rates total flux in the energy bands 26–35 keV and 35–44 keV and from their ratio. This is a much simpler

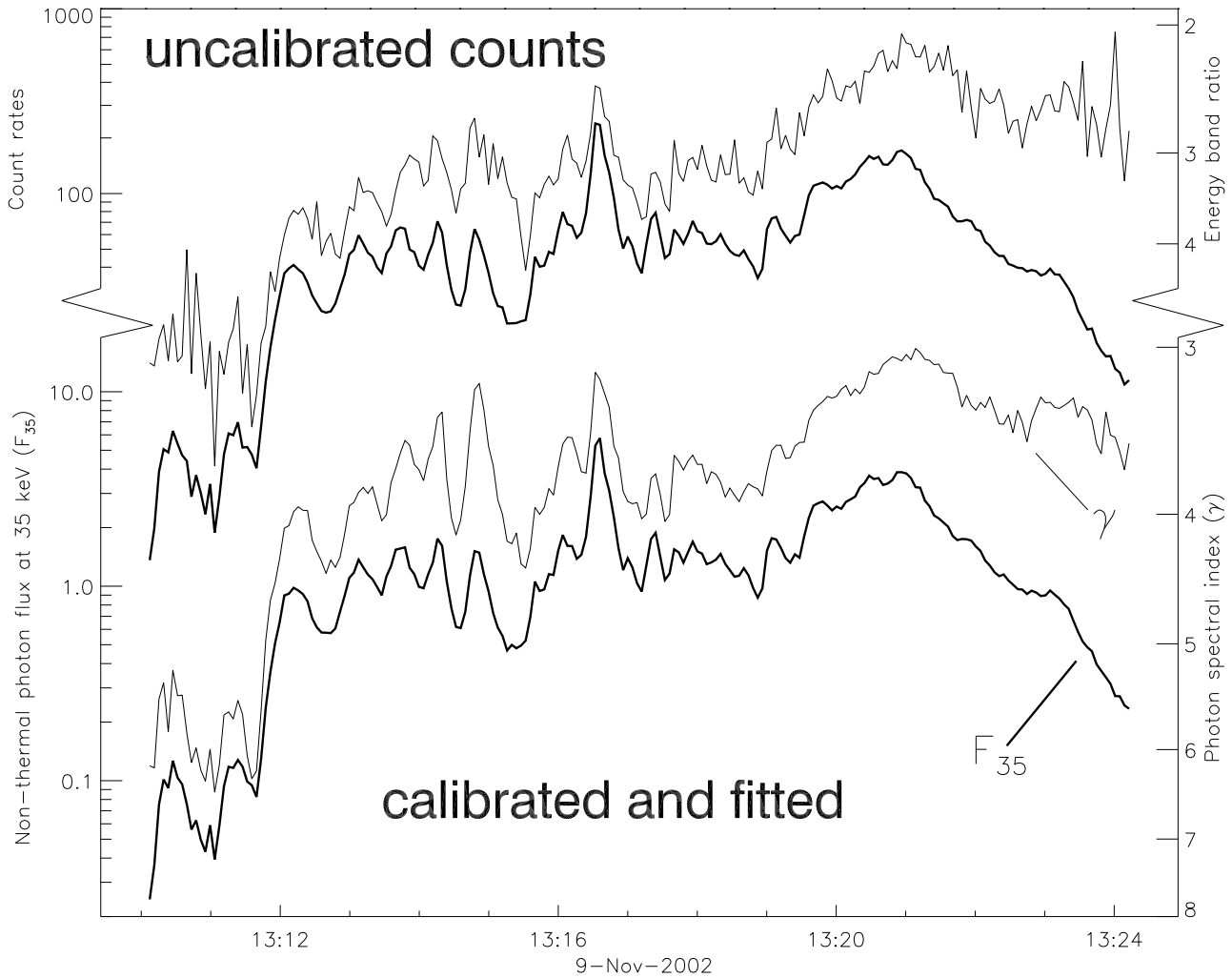


Fig. 2. *Top:* Spectral index (thin line) and flux (thick line) obtained from the uncalibrated total count rates flux in the energy bands 26–35 keV and 35–44 keV and their ratio. *Bottom:* Spectral index γ (thin line) and non-thermal flux F_{35} at 35 keV in photons $\text{s}^{-1}\text{cm}^{-2}\text{keV}^{-1}$ (thick line) for the event of 9 November 2002, obtained by spectral fitting.

and cruder way of determining the values of the two parameters that does not require fitting. Although the absolute values of the parameters will differ, they preserve the temporal variations. Figure 2 shows an extremely close similarity between the uncalibrated count rates in the 26–44 keV energy range and the fitted flux. It proves that the fitting preserves the time evolution of the observed counts with high precision. The spectral ratio derived from uncalibrated counts in the two energy bands is normalized to the energy ranges, but differs from the fitted γ due to the lack of calibration. It is significantly noisier than γ because of the broader energy range used for the fitting, which includes non-thermal photons down to the thermal cross-over near 15 keV. Yet the two spectral parameters follow each other extremely well in time. This confirms that the dependence introduced by fitting is negligible.

To further check that no cross-talk between thermal and non-thermal parameters is introduced by the fitting procedure, we smoothed the curve representing the temperature T as a function of time for flare 23 using a smoothing filter with a time window of 180 s, and recomputed all the fittings forcing

the temperature to follow the smoothed curve. No significant differences were found between the new values obtained for the spectral indices and non-thermal fluxes and the old ones. This shows that any short-term variation of the fitted temperature during an emission peak do not significantly influence the behavior of γ and F_{35} .

3. Relation between flux and spectral index

In this section we will investigate the relation between the spectral index and the non-thermal flux in a quantitative way. For the non-thermal flux there are two options: the strength of the non-thermal flux F_{E_0} at a chosen, fixed normalization energy E_0 or the total non-thermal flux $F_{\text{tot}} = \int F(E) dE$. The first option has the disadvantage of requiring a supplementary arbitrary parameter E_0 . Therefore, it would be conceptually preferable to choose the second. However, the non-thermal flux is only observed in the energy range where it is larger than both the background and the thermal emission. Hence it is not straightforward to compute F_{tot} , because we do not know the

Table 1. List of the selected 24 events. Peak flux means the fitted non-thermal flux at 35 keV at peak time in photons $\text{s}^{-1} \text{cm}^{-2} \text{keV}^{-1}$. The peak time given reflects the time of maximum flux *after* the fitting selection, and may therefore not coincide with the peak of a light curve at 35 keV.

Event Nr.	Event date	Peak time	Peak flux	Peak γ	Number of fittings
1	20 Feb 2002	09:54:04	0.315	6.8	54
2	20 Feb 2002	16:22:58	0.168	3.8	11
3	20 Feb 2002	21:06:05	2.388	4.1	23
4	25 Feb 2002	02:56:42	0.390	5.5	29
5	26 Feb 2002	10:26:52	4.915	3.2	20
6	15 Mar 2002	22:23:06	0.243	4.9	125
7	04 Apr 2002	10:43:55	0.261	5.2	49
8	04 Apr 2002	15:29:16	2.124	4.7	32
9	09 Apr 2002	12:59:51	0.403	4.9	41
10	14 Apr 2002	03:24:44	0.715	4.6	13
11	17 Apr 2002	00:38:34	0.253	4.4	8
12	24 Apr 2002	21:50:23	0.712	4.0	16
13	01 Jun 2002	03:53:41	2.473	3.0	25
14	16 Aug 2002	22:10:30	1.629	4.9	18
15	17 Aug 2002	01:02:04	0.076	4.3	5
16	23 Aug 2002	11:59:05	0.220	6.4	14
17	24 Aug 2002	05:43:23	0.216	5.7	84
18	27 Aug 2002	12:28:38	1.617	3.1	8
19	29 Sep 2002	06:36:18	4.261	3.8	30
20	29 Sep 2002	14:46:43	0.405	3.9	40
21	30 Sep 2002	01:48:25	0.107	7.3	18
22	04 Oct 2002	00:41:13	1.109	4.6	20
23	09 Nov 2002	13:16:36	5.776	3.2	212
24	14 Nov 2002	22:24:40	1.978	3.8	16

non-thermal emission outside the observed range. The main uncertainty in F_{tot} comes from errors in the estimates of the low-energy turnover E_{turn} , especially for steep spectra, where small errors in E_{turn} can produce large changes in F_{tot} . Since spectral fittings are poorly suited to accurately determine E_{turn} and hence F_{tot} (for a detailed discussion, see Saint-Hilaire and Benz, 2004), the large uncertainties in F_{tot} rule out its use as a main parameter for our study. We are left with the first option, but we have to choose E_0 . It should lie in an energy range where the non-thermal emission is actually observed and fitted, to compare observable quantities. The non-thermal emission is best observed and identified in the energy range 20–50 keV, and hence we choose the center $E_0 = 35 \text{ keV}$, and investigate the γ - F_{35} relation. In Section 4 we will consider the implications of changes in E_0 from the chosen 35 keV.

Fig. 3 presents a logarithmic plot of γ versus F_{35} for all of the 911 data points. The plot clearly shows the overall SHS trend. The cross-correlation coefficient of $\ln \gamma$ versus $\ln F_{35}$ is $r = -0.80 \pm 0.03$, where the uncertainties given represent the 99% confidence range. The cross correlation coefficient r is significantly lower than 1 because of the scatter in the data, which is real and not due to measurement errors. The γ vs. F_{35} relation can be approximated by a power-law model

$$\gamma = AF_{35}^{-\alpha} \quad \text{or, equivalently,} \quad (2)$$

$$\ln \gamma = \ln(A) - \alpha \ln F_{35}. \quad (3)$$

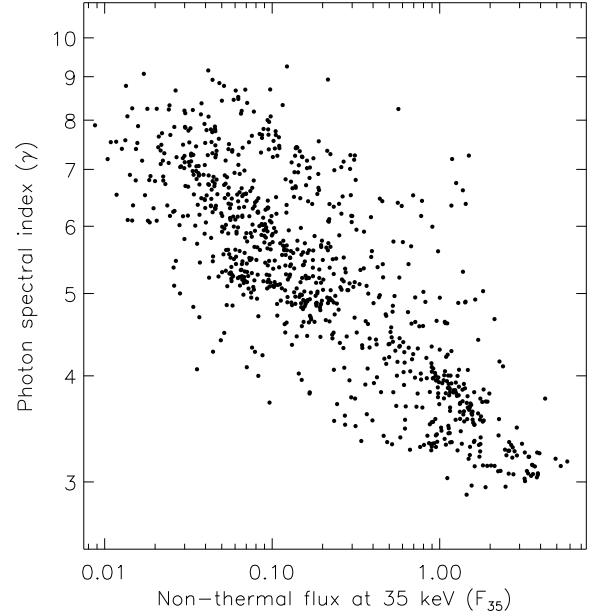


Fig. 3. Plot of γ versus the fitted non-thermal flux at 35 keV (given in photons $\text{s}^{-1} \text{cm}^{-2} \text{keV}^{-1}$). All the 911 data points from the 24 events are shown.

In Eq. (2) and in the following, F_{35} is used as a dimensionless number given by the normalization factor at 35 keV divided by the unit flux ($1 \text{ photon s}^{-1} \text{cm}^{-2} \text{keV}^{-1}$). The constants A and α can be obtained by means of a linear least-squares (LS) regression of the quantities $\ln \gamma$ vs. $\ln F_{35}$. However we note that:

1. The γ - F_{35} data have a fairly large scatter.
2. We have to treat the variables γ and F_{35} symmetrically, since it is not *a priori* clear that one of them is a function of the other, and thus there is no reason to take either one as a *dependent* variable.

In such a case, Isobe et. al. (1990) suggest that the best fitting parameters are obtained by the LS bisector method. The method consists of taking the line that bisects the $\text{LS}(\ln \gamma | \ln F_{35})$ and $\text{LS}(\ln F_{35} | \ln \gamma)$ regression lines, where $\text{LS}(y | x)$ means the least-square regression of the dependent variable y against the independent variable x . The LS bisector gives for our model parameters: $A = 4.043 \pm 0.032$ and $\alpha = 0.197 \pm 0.003$. Computing α by $\text{LS}(\ln \gamma | \ln F_{35})$ we get $\alpha = 0.154 \pm 0.003$, and using $\text{LS}(\ln F_{35} | \ln \gamma)$ $\alpha = 0.241 \pm 0.006$. The latter two values define a confidence range for α , such that $\alpha = 0.20 \pm 0.05$. These values will be refined in the following. They may be used for a future comparison, e.g. with a peak-flux analysis.

The overall behavior of the plot in Fig. 3 results from the superposition of points from different flares. We now want to look in some more detail at the behavior of single flares. Fig. 4 gives the time evolution of γ and F_{35} for 4 flares. Anti-correlation of F_{35} and γ can clearly be seen in all of them. However, it is evident from a close inspection of the light curves that a model of a strict functional dependence like the one of Eq. (2) will

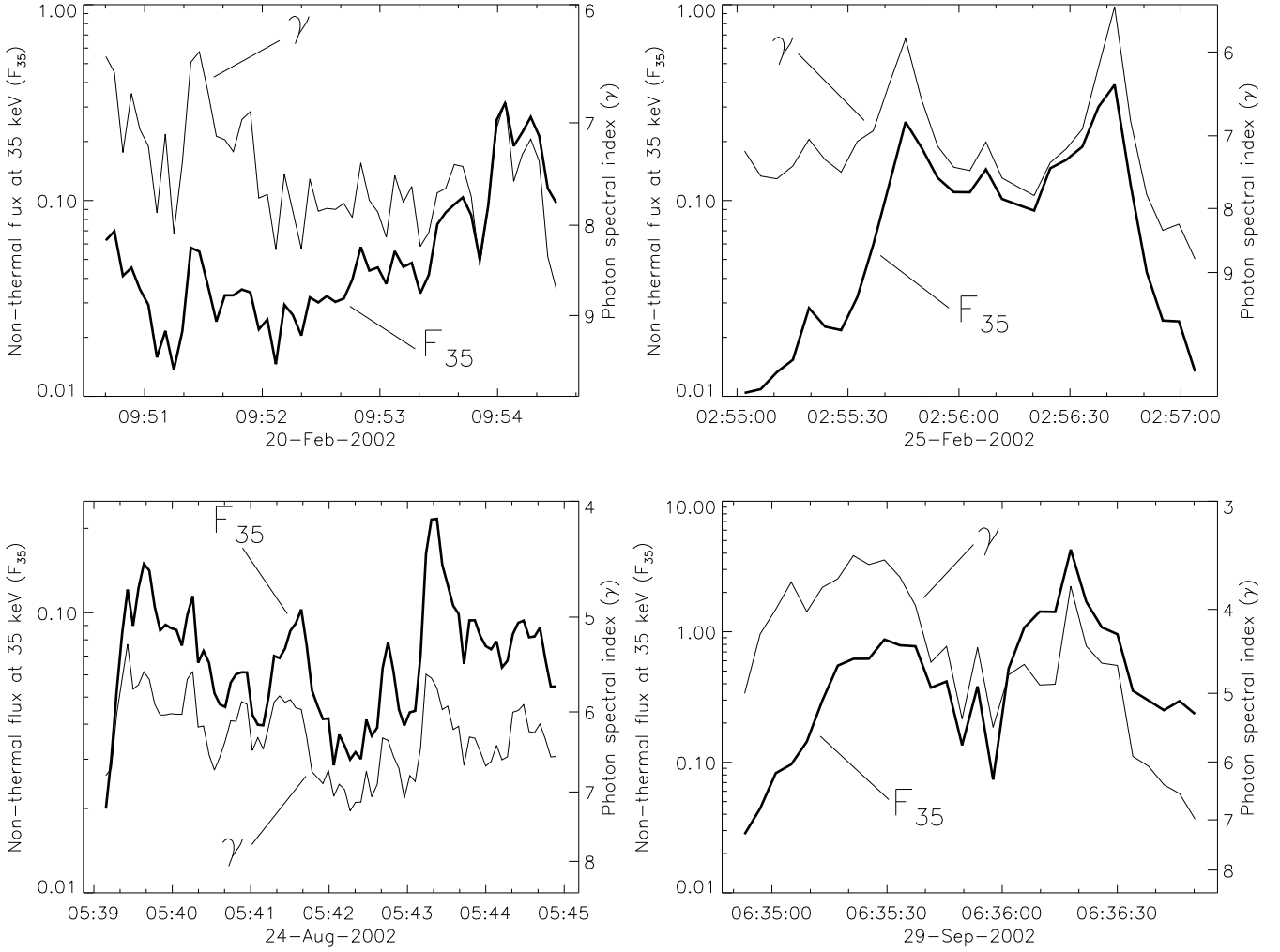


Fig. 4. Time evolution of the photon spectral index γ (thin line) and the non-thermal flux at 35 keV F_{35} (thick line) for 4 flares.

not work well for an entire flare, since there are consecutive peaks in F_{35} with about the same height, but having different minimum values of γ . Nevertheless each peak shows an unmistakable SHS pattern. It seems likely that the proposed power-law model suits better the behavior of single peaks than whole flares. To check this, we computed the vertical scatter of the data points around their $\text{LS}(\ln \gamma | \ln F_{35})$ regression line for the set of all the data points, for the 24 subsets of points belonging to each flare, and for 141 subsets of points belonging to 70 rise and 71 decay phases of peaks during the flares. The rise and decay phases were selected with the requirement that each phase consists of at least 3 consecutive data points. The vertical scatter σ_I of a subset I of n points $(\ln F_{35}^i, \ln \gamma^i)$, $i \in I$ around the straight line defined by Eq. (3) with $\text{LS}(\ln \gamma | \ln F_{35})$ parameters slope α_I and intercept $\ln A_I$ can be computed by

$$\sigma_I^2 = \frac{1}{n-2} \sum_{i=1}^n (\ln \gamma^i - \ln A_I + \alpha_I \ln F_{35}^i)^2, \quad (4)$$

where $n-2$ are the degrees of freedom of the subset with the fitted straight line. For the set of all 911 points $\sigma = 0.165$. The average of σ computed for each single flare is 0.094. The

average of σ for each rise and decay phase is 0.020 and, respectively, 0.017. The improvement in sigma going from the total dataset to the flares and then to the rise/decay phases shows that indeed single peaks are better represented by the model, in the sense that they have much less vertical scatter around the regression line.

Fig. 5 shows the γ vs. F_{35} plot for three events. For each flare, the points belonging to the longest rise (top row) and decay (bottom row) phase are represented by pluses and their $\text{LS}(\ln \gamma | \ln F_{35})$ regression line is drawn. Since here we have much less scatter, there is little difference between the different LS regression schemes. It can be seen that the scatter around the fitted line is low during the rise/decay phases. Interestingly, in some flares the fitted line is steeper in the decay phases.

We show the distribution of the slope of the fitted lines in Fig. 6. The bin width is 0.5 standard deviations of the measured slopes. The average value for the rise phase is

$$\alpha_r = 0.121 \pm 0.009 \quad (5)$$

and the one for the decay phase is

$$\alpha_d = 0.172 \pm 0.012. \quad (6)$$

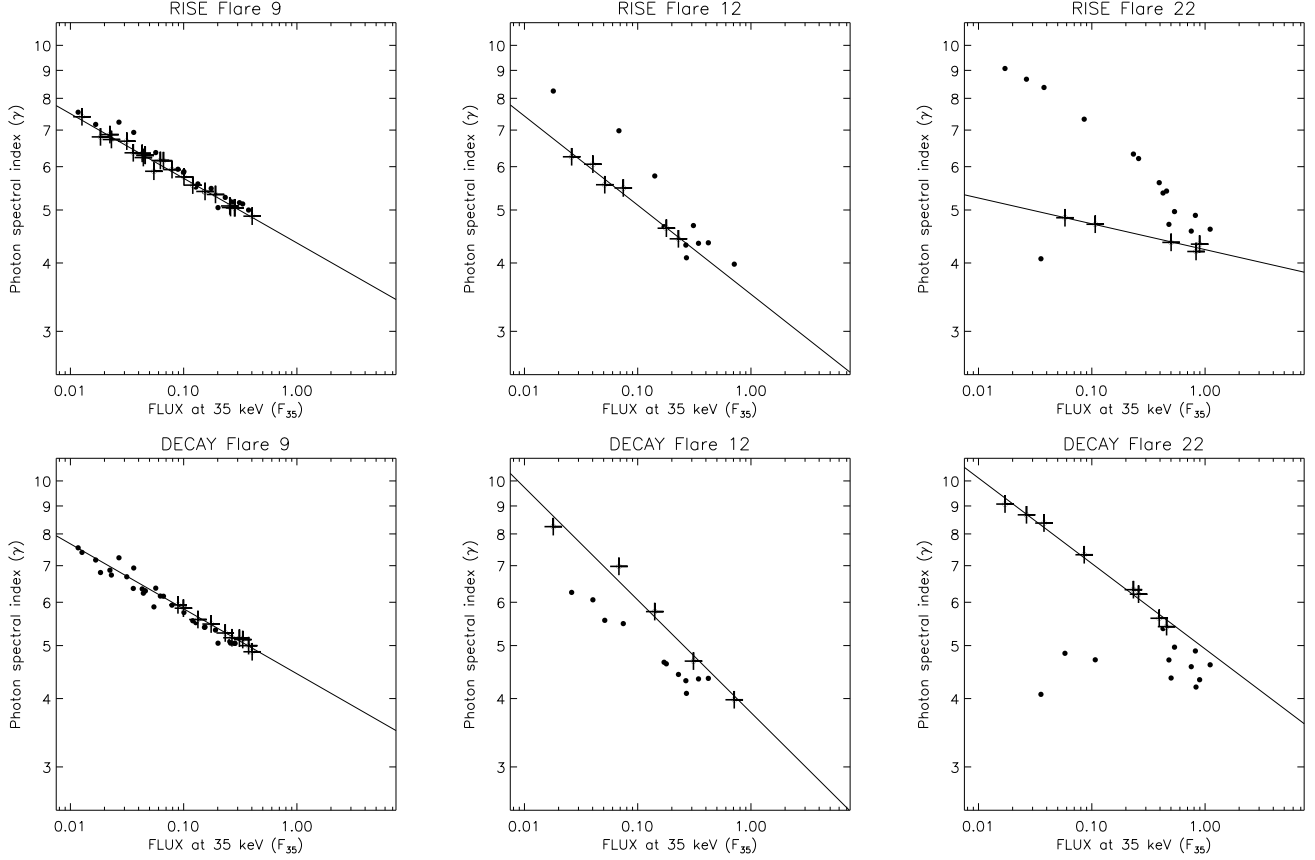


Fig. 5. Spectral index γ versus flux at 35 keV F_{35} for 3 flares. The plus signs in the top and bottom row of plots mark the points forming the longest uninterrupted rise and decay phase in the flare. The regression line of the selected data points is shown.

The standard deviations are $\sigma_r = 0.073$ and $\sigma_d = 0.103$, respectively.

The difference in averages is about 5 times the standard errors of the mean, and therefore the difference between the two cases is statistically significant. We see that for most of the rise phases there is a soft-hard trend (negative slope) and for most of the decay phases there is a hard-soft trend (also described by a negative slope). The number of rise phases with slope smaller than 0.04 are 5 out of 70, and the number of decay phases with slope smaller than 0.04 are 2 out of 71. Therefore the SHS behavior is a nearly universal trend in peaks of non-thermal emission.

We also investigated whether there is a significant delay in the correlation of F_{35} and γ . We defined the delay as the time of the minimum of the quadratic interpolation curve going through the 3 cross-correlation coefficients corresponding to a lag of -1 , 0 and 1 time bins of about 4 seconds. The interpolation enhances considerably the time resolution, as the noise is small. The distribution of the delays is relatively broad, centered at -0.32 s, with a standard deviation of 1.1 s and with extreme delays up to ± 3 s. The average of the delays does not significantly differ from 0 since the standard error of the mean is ± 0.23 s.

Furthermore, we tried to see if there is any evidence in the data for the presence of a *pivot point*, i.e. a fixed point with coordinates (E^*, F^*) common to all the spectra in a rise/decay

phase. We note that such a concept corresponds to a model that does not yield a power-law dependence of F_{35} and γ , but instead

$$\gamma = -\frac{\ln(F^*/F_{35})}{\ln(35\text{keV}/E^*)}, \quad (7)$$

contrary to Eq. (2). We computed the intersections of the power-law fits to the non-thermal component of the photon spectrum of all 4 s time bins in each rise phase of every flare with all other non-thermal components in the same phase. While this procedure is quite sensitive to errors for nearly parallel lines, the total distribution yields a clue whether there is any virtue in the idea of a pivot point. The energy distribution of the intersections peaks around 9 keV, and was larger than half of the maximum in the energy range 6.5–12.5 keV, but it had comparatively large tails to very low and very high energies. There seems to be no real pivot point, but the region of intersection is relatively narrow. Therefore, when trying to visualize the time evolution of the non-thermal spectrum during the rise phase, one does not too badly by imaging the spectrum as fixed at an energy around 10 keV. In the course of the flare the non-thermal spectrum rises its high-energy tail until peak time, and it lowers it again afterwards.

4. Discussion

The power-law model for the γ - F_{35} relation is admittedly very simple, yet it provides a good empirical description of the ob-

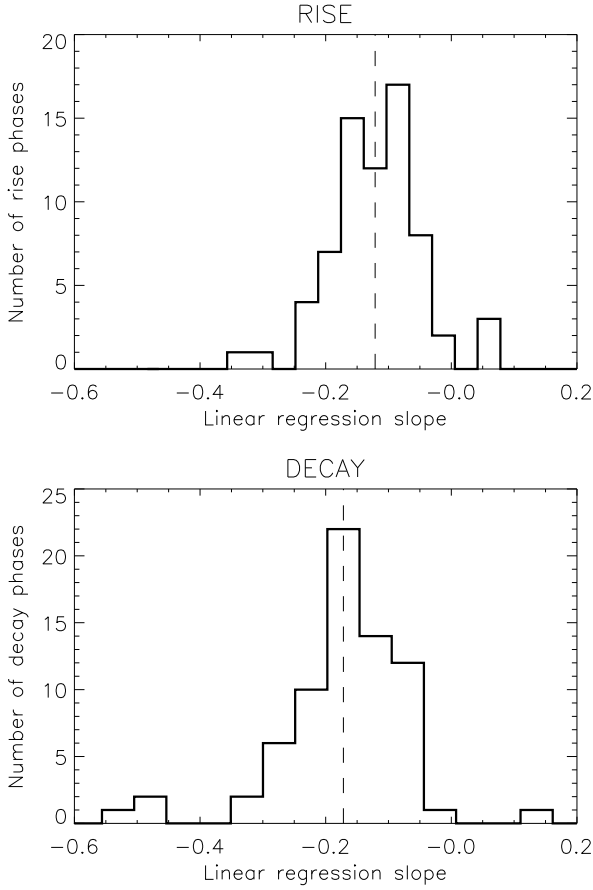


Fig. 6. Distribution of the linear regression slopes for the rise and decay phases. The average value is marked by the dashed line.

served quantities. The range of validity of the model is limited at very high flux values, since γ has a theoretical lower limit at roughly 1.4, given by the bremsstrahlung of a monoenergetic beam. Its major disadvantage is the arbitrary assumption of a normalization energy, here 35 keV. How do the results shown in Section 3 depend on the choice $E_0 = 35$ keV?

Let E_1 and $E_2 = E_1 + \Delta E$ be two normalization energies. The normalization coefficients F_{E_0} and F_{E_1} satisfy

$$F_2 = F_1 \left(\frac{E_2}{E_1} \right)^{-\gamma}. \quad (8)$$

Now let us assume that the relation $\gamma = A_1 F_1^{-\alpha_1}$ holds. Using Eq. (8), this can be written as

$$\ln \gamma = \ln A_1 - \alpha_1 \ln F_2 - \alpha_1 \gamma \ln \frac{E_2}{E_1}. \quad (9)$$

If $\Delta E/E_1 \ll 1$, we can expand the logarithm and get

$$\ln \gamma = \ln A_1 - \alpha_1 \ln F_2 - \alpha_1 \gamma \frac{\Delta E}{E_1}. \quad (10)$$

The logarithmic derivative of this expression yields

$$\frac{d \ln \gamma}{d \ln F_2} = \frac{-\alpha_1}{1 + \alpha_1 \gamma \frac{\Delta E}{E_1}} \approx -\alpha_1 \left(1 - \alpha_1 \gamma \frac{\Delta E}{E_1} \right). \quad (11)$$

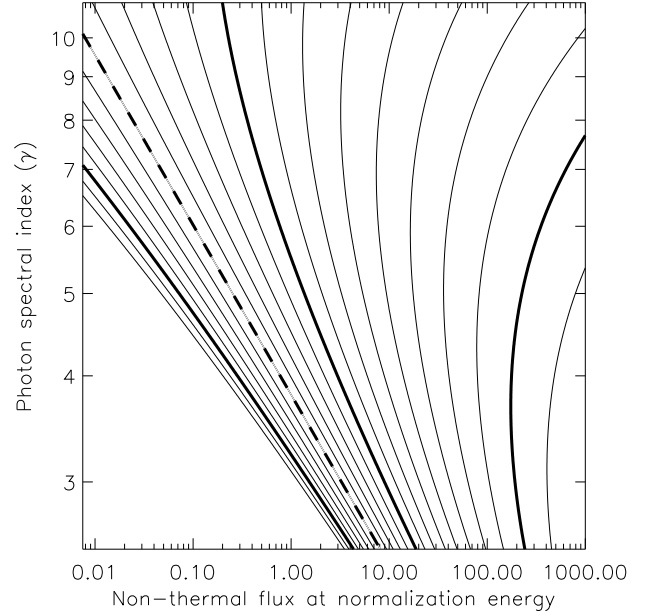


Fig. 7. The lines shown here model the relation between the spectral index γ and the non-thermal flux F_{E_0} at different energies E_0 , assuming that $\gamma = A F_{35}^{-\alpha}$ holds at $E_0 = 35$ keV with $\alpha = 0.2$ and $A = 3.8$. The dashed line corresponds to $E_0 = 35$ keV, the lower thick line to $E_0 = 45$ keV, the upper thick line to, respectively, $E_0 = 25$ keV and $E_0 = 9$ keV. The separation between thin lines is 2 keV.

The $\ln \gamma - \ln F_{E_2}$ relation is not linear, as γ appears on the right hand side of Eq. (11). If a new exponent α_2 were fitted to the $\ln \gamma - \ln F_{E_2}$ data points, we would get according to Eq. (11),

$$\alpha_2 \approx \alpha_1 \left(1 - \alpha_1 \gamma \frac{\Delta E}{E_1} \right). \quad (12)$$

For $\Delta E \ll E_1$ the relation between $\ln \gamma_2$ and $\ln F_{E_2}$ is still approximately linear but flatter than for $\ln F_{E_1}$ if $\Delta E > 0$. This is confirmed in Fig. 7, where the γ vs. F_{E_0} relation is shown for different normalization energies E_0 . In Fig. 7 the $\gamma - F_E$ relation is presented according to Eq. (9). In the course of a subpeak the spectral index and flux move approximately on one of the lines according to the given normalization energy, assuming the relation (2). The relation steepens with decreasing normalization energy E_0 and finally turns over. In a model with a pivot point at energy E^* the $\gamma - F_{E_0}$ relation would be a vertical line for $E = E^*$.

The final goal (not part of this paper) is the comparison of these results with the prediction of theoretical models for the energy distribution of accelerated electrons. For this purpose the electron distribution needs to be reconstructed from the observed photon spectrum. As an example, the analytically solvable thick target impact model using the non-relativistic Bethe-Heitler cross section (Brown 1971, Tandberg-Hanssen and Emslie 1988) predicts that an electron power-law distribution $\Phi(\epsilon) = \Phi_{\epsilon_0} (\epsilon/\epsilon_0)^{-\delta}$ [electrons $\text{s}^{-1} \text{keV}^{-1}$] generates a pho-

ton spectrum $F(E) = F_{E_0}(E/E_0)^{-\gamma}$ [photons $\text{s}^{-1} \text{cm}^{-2} \text{keV}^{-1}$] with

$$\delta = \gamma + 1 \quad (13)$$

and

$$\Phi_{e_0} = K F_{E_0} E_0^\gamma \epsilon_0^{-\delta} \frac{(\delta - 1)(\delta - 2)}{\beta(\delta - 2, 1/2)}, \quad (14)$$

where $\beta(x, y)$ is the beta function and the constant K is given by

$$K = \frac{3\pi^2 e^4 \ln \Lambda D^2}{Z^2 \alpha r_e^2 m_e c^2} \approx 6.6 \cdot 10^{33} \text{ keV cm}^2, \quad (15)$$

where $\ln \Lambda$ is the Coulomb logarithm, D the distance from the target (here 1 AU), Z the average atomic number, α the fine structure constant and r_e the classical electron radius. Eq. (14) indicates that the relation between electron flux and gamma will not conserve linearity in the log-log representation. In other words, the assumed linear relation for fitting photons must be considered as a convenient but rather arbitrary approximation.

5. Conclusion

This study of the γ - F relation in the evolution of the non-thermal component of impulsive solar flare hard X-ray emissions exploits the high spectral resolution of the RHESSI germanium detectors. Contrary to earlier investigations, the spectral index is not derived from the ratio of a few channels, but from fitting the spectrum at relatively low non-thermal energies where most of the photons are emitted. This method eliminates the influence of the thermal component and improves considerably the noise on the derived spectral index (Fig. 1).

The most surprising result of the improved accuracy is the appearance of the soft-hard-soft behavior on short time scales. The SHS behavior is a feature seen in nearly all of the non-thermal emission peaks of M-class solar flares. Whereas SHS was previously considered to be a global property of flares, Figs. 2 and 4 demonstrate that SHS is a predominantly short-scale phenomenon. This is the reason why the scatter in the γ - F_{35} plot diminishes when rise and decay phases of individual subpeaks are analyzed separately.

The novel quantitative analysis of the γ - F_{35} relation has also revealed remarkable properties. The relation appears linear in double-logarithmic representation (Fig. 3). Thus it follows an approximate power law, $\gamma = AF_{35}^{-\alpha}$. Its average index α is 0.197 ± 0.003 . The scatter is greatly reduced if individual subpeaks are studied (Fig. 5). In the rise phase of individual flare elements, the average index $\alpha_r = 0.12 \pm 0.01$ is significantly smaller than the index of the decay phase $\alpha_d = 0.17 \pm 0.01$ (Fig. 6). The path of a subpeak in the γ - F_{35} plot (Fig. 5) follows tententially a slanted V, with the rise phase forming the flatter leg. This amounts to a secondary trend, superimposed on the SHS behaviour, of a general spectral softening of the non-thermal component in the course of a subpeak.

The SHS behavior supports the idea that each non-thermal emission peak represents a distinct acceleration event of the

electrons in the flare. The individual peaks mainly differ by their value for A in the $\gamma = AF_{35}^{-\alpha}$ relation, presumably due to different physical parameters in the acceleration region.

It is possible to visualize the γ - F_{35} relation by a pivot point in the non-thermal spectrum. This point is relatively stable in energy and flux. The pivot energy was determined as 9 keV in the average with a half-power distribution of 6.5–12.5 keV. In the course of a peak, the non-thermal spectrum rises by turning around the pivot point, decreasing γ and increasing the flux beyond the energy of the pivot point. In the decay phase the spectrum decreases and turns the opposite way. The picture is supported by the observations of no delay (in the average). We note, however, that the pivot point model is only an approximation and needs to be further investigated.

The SHS phenomenon of flares, and in particular of subpeaks, contradicts the idea of the statistical flare in avalanche models (Lu & Hamilton 1991), assuming that each flare and subpeak is composed of many identical elements that are far below resolution. The superposition of such subresolution structures in a straightforward avalanche process would not yield the observed SHS time behavior.

The subpeaks defined by the SHS behavior thus may be considered as irreducible flare elements. They have durations of one minute (Fig. 2) to shorter than 8 seconds, the lower limit given by the time resolution (Fig. 4). The close correlation suggests that there is an intrinsic dependence between the flux and energy distribution of electrons for any given elementary acceleration event. If this is the case, it implies that individual SHS structures cannot be further resolved, thus form the elementary structures of flares.

Acknowledgements. The analysis of RHESSI data at ETH Zurich is partially supported by the Swiss National Science Foundation (grant nr. 20-67995.02). This work relied on the RHESSI Experimental Data Center (HEDC) supported by ETH Zurich (grant TH-W1/99-2). We thank the many people who have contributed to the successful operation of RHESSI. We acknowledge the contribution of D. Buser, who has prepared the ground for this work in his Diploma Thesis (2003). We thank P. Saint-Hilaire, K. Arzner, S. Krucker, R. Schwartz and H. Hudson for helpful discussions, and the referee for constructive comments.

References

- Benz, A. O. 1977, ApJ, 211, 270
- Brown, J. C. 1971, Sol. Phys., 18, 489
- Brown, J. C., Emslie, A. G., & Kontar, E. P. 2003, ApJ, 595, L115
- Brown, J. C., & Loran, J. M. 1985, MNRAS, 212, 245
- Buser, D. 2003, Diploma Thesis, <http://e-collection.ethbib.ethz.ch/show?type=dipl&nr=106>
- Cliver, E. W., Dennis, B. R., Kiplinger, A. L., et al. 1986, ApJ, 305, 920
- Dennis, B. R. 1985, Sol. Phys., 100, 465
- Fivian, M., Hemmeck, R., Mchedlishvili, A., & Zehnder, A. 2002, Sol. Phys., 210, 87
- Fletcher, L. & Hudson, H. S. 2002, Sol. Phys., 210, 307
- Frost, K. J., & Dennis, B. R. 1971, ApJ, 165, 655
- Hudson, H. S. & Fárník, F. 2002, ESA SP-506: Solar Variability: From Core to Outer Frontiers, 261
- Hurford, G. J., & Curtis, D. W., Sol. Phys., 210, 101

- Isobe, T., Feigelson, E. D., Akritas, M. G., & Babu, G. J. 1990, *ApJ*, 364, 104
- Kane, S. R., & Anderson, K. A. 1970, *ApJ*, 162, 1003
- Kiplinger, A. L. 1995, *ApJ*, 453, 973
- Lin, R. P. & Schwartz, R. A. 1986, *ApJ*, 312, 462
- Lin, R. P., Dennis, B. R., Hurford, G. J., et al. 2002, *Sol. Phys.*, 210, 3
- Lu, E. T. & Hamilton, R. J. 1991, *ApJ*, 380, L89
- Parks, G. K. & Winckler, J. R. 1969, *ApJ*, 155, 117
- Saint-Hilaire, P., Von Praun, C., Stolte, E., et al. 2002 *Sol. Phys.*, 210, 143
- Saint-Hilaire & Benz, A. O. 2004, to be submitted to *A&A*
- Schwartz, R. A. 1996, 'Compton Gamma Ray Observatory Phase 4 Guest Investigator Program: Solar Flare Hard X-ray Spectroscopy', Technical Report, NASA Goddard Space Flight Center.
- Smith, D. M., Lin, R. P., Turin, P., et al. 2002, *Sol. Phys.*, 210, 33
- Tandberg-Hanssen, E. & Emslie, A. G., 'The physics of solar flares', Cambridge University Press, 1988